



Nano silica extracted from horsetail plant as a natural silica support for the synthesis of $\text{H}_3\text{PW}_{12}\text{O}_{40}$ immobilized on aminated magnetic nanoparticles ($\text{Fe}_3\text{O}_4@\text{SiO}_2\text{-EP-NH-HPA}$): a novel and efficient heterogeneous nanocatalyst for the green one-pot synthesis of pyrano[2,3-*c*]pyrazole derivatives

Nina Hosseini Mohtasham¹ · Mostafa Gholizadeh¹ 

Received: 4 December 2019 / Accepted: 19 March 2020
© Springer Nature B.V. 2020

Abstract

In this work, nanomesoporous silica has been prepared from horsetail (*Equisetum arvense*), which is a medicinal plant, with high surface area. This natural silica has been applied as a support to prepare $\text{H}_3\text{PW}_{12}\text{O}_{40}$ immobilized on aminated epibromohydrin-functionalized $\text{Fe}_3\text{O}_4@\text{SiO}_2$ nanoparticles ($\text{Fe}_3\text{O}_4@\text{SiO}_2\text{-EP-NH-HPA}$) as a highly powerful magnetically solid acid catalyst. Characterization of this nanocatalyst has been investigated by a variety of techniques such as FTIR, XRD, N_2 adsorption–desorption, TEM, SEM–EDX, TGA, VSM, ICP–OES and elemental analysis. This magnetically solid acid nanocatalyst has been successfully used for the one-pot green synthesis of pyrano[2,3-*c*]pyrazole derivatives in an aqueous medium at room temperature. The procedure resulted in structurally different pyrano[2,3-*c*]pyrazoles in excellent yields in very low reaction times. Moreover, this magnetically solid acid nanocatalyst can be simply recovered by an external magnetic field and reused for seven consecutive reaction cycles without significant loss of activity.

Graphic abstract

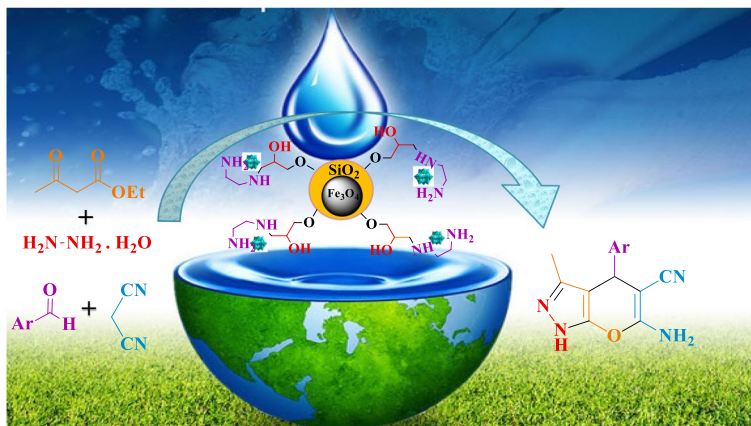
In this work, $\text{Fe}_3\text{O}_4@\text{SiO}_2\text{-EP-NH-HPA}$ as a highly powerful magnetically solid acid nanocatalyst based on natural silica which was extracted from a medicinal plant

Electronic supplementary material The online version of this article (<https://doi.org/10.1007/s11164-020-04133-8>) contains supplementary material, which is available to authorized users.

✉ Mostafa Gholizadeh
m_gholizadeh@um.ac.ir

¹ Department of Chemistry, Faculty of science, Ferdowsi University of Mashhad, Mashhad, Iran

was prepared and characterized using various techniques. The activity of the new catalyst was tested for the synthesis of pyrano[2,3-*c*]pyrazole derivatives.



Keywords Horsetail plant · Natural silica · Heteropolyacid · Heterogeneous catalyst · Pyrano[2,3-*c*]pyrazoles

Introduction

According to the “green and sustainable chemistry,” the application of the environmentally benign reagents and reaction conditions is one of the most pleasing developments in synthetic organic chemistry [1]. The green catalytic protocols and environmentally friendly reaction conditions in which the use of volatile organic solvents, toxic reagents, hazardous or harsh reaction conditions as well as challenging and time-consuming wasteful separations has been avoided are of significant importance to the chemists who make scientific efforts to avoid the annihilation of our blue planet for a sustainable future [2]. Hence, the improvement in a novel, eco-friendly, nontoxic, inexpensive, stable and recyclable catalysts with improved efficiency has drawn a great deal of attention, regarding the green chemistry demands [3–5]. Keggin-type heteropolyacids (HPAs), specifically $\text{H}_3\text{PW}_{12}\text{O}_{40}$, have attracted more attention due to their great acidity, high catalytic activity and low toxicity leading to be known as eco-friendly compounds [6]. Nevertheless, owing to their homogeneous structure, these compounds show some limitations in their catalytic activity and separation from the reaction mixture, which are identified as poor stability and high solubility in polar solvents [7]. Besides the formation of immense amounts of waste products, these disadvantages lead to wasting energy which is not in accordance with the concept of “Green Chemistry.” Therefore, the heterogenization of these homogeneous catalysts through their immobilization on various solid supports has been developed as a main solution to overcome the problems caused by such catalysts [8, 9].

However, structural modifications of the HPAs on the solid supports such as silica, carbon nanotube, titania and alumina which circumvent some of these problems have also been reported [10–18]. This process leads to the improvement in the aspect of environmental compatibility, as well as economic aspect, in numerous industrial manufacturing processes.

The unique properties of magnetite nanoparticles (Fe_3O_4) including potentiality for large-scale production with low cost, high thermal and mechanical stability have aroused a notably interest in the past decade. Understandably, their paramagnetic structure allows simple and efficient separation from the reaction mixture which skips over the standard filtration required in the separation of heterogeneous catalysts. Magnetite nanoparticles (Fe_3O_4) can be separated from the reaction mixture using an external magnet [19]. However, the implication of magnetic nanoparticles has some problems, one of which is known as agglomeration [20]. Pleasantly, this can be avoided by coating the catalyst surface with various organic or inorganic shells including silica, polymers, biomolecules, metals, etc. [21, 22], among which silica is the best choice due to its inherent properties such as thermal stability against degradation, biocompatibility and high stability in aqueous media, besides presenting a preferable surface area and therefore desirable loading of active sites [23]. Nowadays, sol–gel processing or vapor-phase reaction using silicon alkoxides such as TEOS (tetraethyl orthosilicate)/TMOS (tetramethyl orthosilicate) as preceding materials is almost used to produce silica powders with extremely high level of purity [24]. However, their preparations including the initial precursors are very expensive, which results in their extreme usage limitation. Silica-rich plant materials such as rice husk [25], wheat hull and wheat hull ash [26], bagasse ash [27], lemon grass [28], etc., can be used as an alternative to prepare nanometer-size and highly purified silica based on high volume and low cost in an almost amorphous form. Therefore, it is considered as a cheap, highly reactive silicon source for the production of various silicon-based materials with new properties, which may be of technical and industrial importance. Due to the presence of silica in association with organic tissue, such as polysaccharides or proteins in these plants, an appropriate strategy is required to extract silica from plant materials with specific characteristics (for instance, having large surface area and high porosity in comparison with the native plant itself). Horsetail can be approximately defined as a field of *Equisetum arvense* and is a widely distributed plant in almost all parts of the world [29], and it is known as one of the most densely silicified plants in which silica is deposited mostly in amorphous form [30] (Scheme 1). For decades, horsetail which is believed to have some medicinal properties due to its high silica content has been extensively applied in medicine [31–33].

Having attracted enormous attention in recent years, multicomponent reactions (MCRs) are one-pot processes in which three or more components come together to form a product containing substantial elements of all the reactants [34]. This approach brings about especial advantages over common reactions, due to the convergence, inherent atom economy, operational simplicity and shortness of their synthetic pathway [35]. These reactions have recently acquired a new dimension to present an invaluable protocol for the formation of massive libraries of drugs such as compounds and drug discovery developments [36].

Scheme 1 Image of the horse-tail plant



Pyrano-pyrazole derivatives which include wide range of biological activities such as exhibiting analgesic, anti-inflammatory potencies as well as being re-known as vasodilators, hypotensive and hypoglycemic agents have been in focus of significant research by scientists [37, 38].

In the current research after reviewing the functionalized magnetic nanoparticles and also their efficient use as a magnetically separable catalyst, pure SiO_2 having herbal origin has been directly extracted from horsetail plant and was used for the first time as natural mesoporous silica support. As a result, acidic-functionalized magnetite nanoparticles have been studied and $\text{H}_3\text{PW}_{12}\text{O}_{40}$ has been immobilized over amine-functionalized $\text{Fe}_3\text{O}_4@\text{SiO}_2$ nanoparticles, which increased its activity in comparison with pure $\text{H}_3\text{PW}_{12}\text{O}_{40}$. Consequently, the catalytic scope of $\text{Fe}_3\text{O}_4@\text{SiO}_2\text{-EP-NH-HPA}$ as a newly prepared magnetically nanocatalyst has been examined in the synthesis of pyrano[2,3-*c*]pyrazole derivatives via one-pot multicomponent reactions using ethyl acetoacetate, hydrazine hydrate, various aromatic aldehydes and malononitrile as starting materials.

Notably, the present study aimed to improve the catalytic properties of heteropolyacid with the use of natural silica as support and to show the high performance of $\text{Fe}_3\text{O}_4@\text{SiO}_2\text{-EP-NH-HPA}$ as a reusable solid acid nanocatalyst, which furnished a green and suitable strategy for synthesis of pyrano[2,3-*c*]pyrazole derivatives in short reaction times.

Experimental section

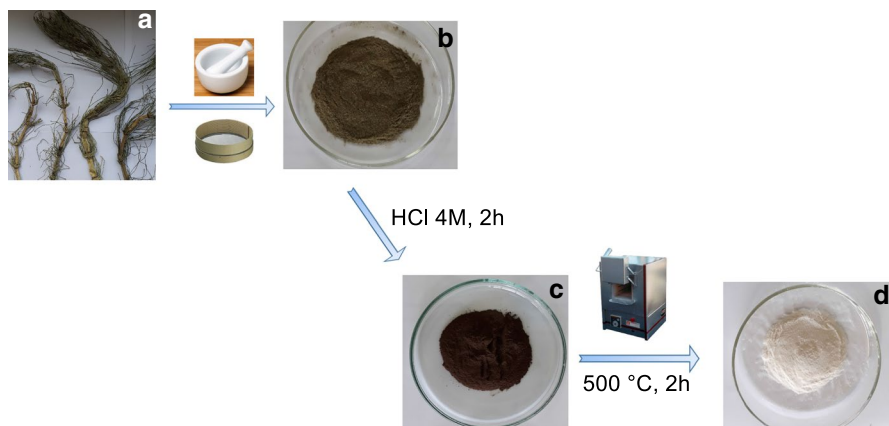
Materials and instruments

All chemical reagents and solvents were purchased from Merck and Sigma-Aldrich chemical companies and used without further purification. All reactions and the purity of obtained products were monitored by thin-layer chromatography (TLC) utilizing aluminum plates coated with silica gel polygram STL G/UV 254 (Merck) using *n*-hexane and ethyl acetate as eluents. The melting points of products were determined with an electrothermal type 9100 melting point apparatus. Mass analysis was performed by Agilent technology (HP) 5973, mass spectrometer operating at an ionization potential of 70 eV. The ^1H NMR and ^{13}C NMR spectra were recorded on a Bruker Avance, at 300 and 75 MHz, respectively, using TMS as an internal standard and DMSO- d_6 as the solvent. The Fourier-transform infrared (FTIR) spectra were recorded from KBr disk within the region range of 400–4000 cm^{-1} using an Avatar 370 FTIR Thermo Nicolet spectrometer. Wide-angle powder X-ray diffraction (XRD) patterns were obtained on a PANalytical Company X'Pert Pro MPD diffractometer with Cu Ka ($\lambda=0.154$ nm) X-ray irradiation source in a 2θ range between 10° and 80° . Surface areas of the samples were measured by adsorption of nitrogen gas at 77 K and the application of Brunauer–Emmett–Teller (BET) calculation, whereas pore size and pore-size distribution were determined using the methods proposed by Barrett, Joyner and Halenda (BJH) and by Dollimore and Heal (DH). A transmission electron microscope (TEM) was conducted on a Leo 912 AB microscope (Zeiss, Germany) operated at 120 kV. Scanning electron microscopy (SEM) images were taken using Leo1450 VP scanning electron microscope operating at an acceleration voltage 20 kV. Elemental compositions were determined with an SC7620 energy-dispersive X-ray analysis (EDX) presenting a 133 eV resolution at 20 kV. Thermal stability of the catalyst was investigated by thermogravimetric analysis (TGA) using a Bahr STA-503 instrument at a heating rate of $10^\circ\text{C min}^{-1}$ under air atmosphere. The magnetic property of catalyst was recorded by the vibrational sampling magnetometry (VSM) technique in 1.5 T external magnetic fields at room temperature, by using magnetic Danesh Pajouh instrument. Inductively coupled plasma optical emission spectroscopy (ICP-OES) was carried out on a 76004555 SPECTRO ARCOS ICP-OES analyzer. All yields refer to isolated products after purification by recrystallization.

Catalyst preparation

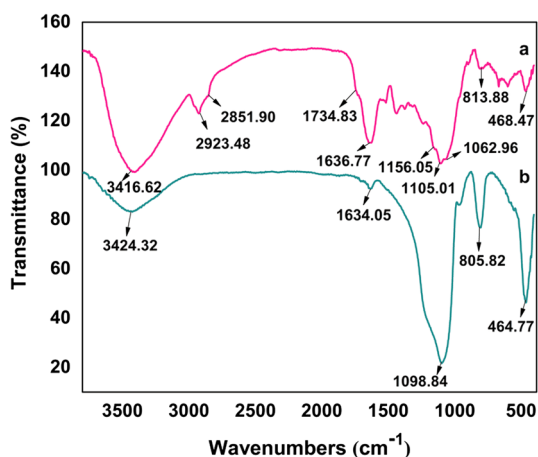
Preparation of silica from horsetail plant

Horsetail plant was purchased from the market, Iran, Mashhad, washed several times with distilled water to remove any adhering and cleaving materials and dried at room temperature for 24 h. Then, the dried plant was smashed and sieved (80 mesh size), again washed with distilled water and dried at 110°C for 5 h.



Scheme 2 Preparation of silica from horsetail plant, a) native horsetail plant, b) horsetail plant after being smashed and sieved (80 mesh size) as green powder, c) sieved horsetail after treatment with HCl as brown powder and d) extracted silica as white color ash

Fig. 1 FTIR spectrum of **a** horsetail plant and **b** isolated silica



Subsequently, purified powdered horsetail (8 g) was taken in a round-bottom flask and 400 mL 4 M hydrochloric acid was added to it. The resulting dispersion was refluxed for 2 h at boiling temperature to remove all inorganic substances except silica. After cooling, the supernatant liquid was discarded and the HCl-treated horsetail was repeatedly centrifuged and washed with deionized water until the pH of the water became nearly 7. The resulting mass was dried in an air oven at 50 ± 5 °C followed by the calcination process to completely remove the organic components. The calcination was carried out in the air atmosphere with a heating rate of 1 K/min and 2 h holding time at 500 °C [29] (Scheme 2). The synthesis of natural pure silica was successfully confirmed with FTIR and EDX analysis (Figs. 1 and 9, respectively).

Preparation of Fe_3O_4 magnetic nanoparticles supported on extracted silica

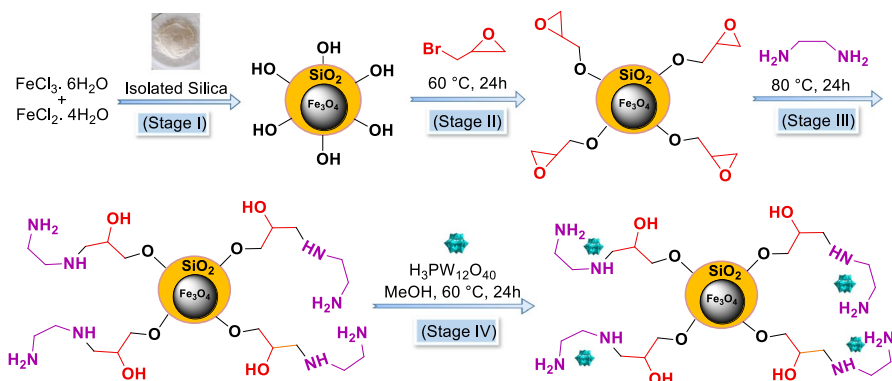
In a typical synthesis, 2 g of natural synthesized silica was dispersed in 60 mL of deionized water in a beaker and $\text{FeCl}_3 \cdot 6\text{H}_2\text{O}$ (5 g) and $\text{FeCl}_2 \cdot 4\text{H}_2\text{O}$ (2 g) were slowly added to it. The mixture was stirred strongly at 80 °C to obtain a clear solution, and then aqueous ammonia was added to it until the pH of 12 was obtained. The solution was kept at 80 °C under vigorous stirring for further 30 min. After that, a bar magnet was held at the bottom of the beaker and all the nanoparticles got stuck to the bottom, and the aqueous part was poured out. By using this technique, the nanoparticles were washed repeatedly with deionized water and finally dried in vacuum at 50 °C for 6 h. The material was designated as Fe_3O_4 @silica (see scheme 3, Stage I).

Preparation of epibromohydrin-functionalized Fe_3O_4 @ SiO_2

Fe_3O_4 @ SiO_2 NPs (1 g) was dispersed in 6 mL pure epibromohydrin by sonication for 30 min. The mixture was heated at 60 °C with vigorous stirring. After 24 h, the epibromohydrin-functionalized Fe_3O_4 @ SiO_2 was separated by an external magnet and washed with MeOH (5 × 10 mL) until the additional amount of epibromohydrin was removed. Then, the obtained Fe_3O_4 @ SiO_2 -EP was dried at 40 °C under vacuum for 18 h (Scheme 3, Stage II).

Preparation of ethylenediamine immobilized on epibromohydrin-functionalized Fe_3O_4 @ SiO_2

To a suspension of Fe_3O_4 @ SiO_2 -EP (1 g) in 50 mL toluene, ethylenediamine (5 mL) was added. The resulting mixture was stirred at 80 °C for 24 h. After completion, the resulting Fe_3O_4 @ SiO_2 -EP-NH as a dark-brown precipitate was separated by an external magnet, washed with MeOH and dried at 80 °C for 14 h (Scheme 3, Stage III).



Scheme 3 Schematic representation of the synthesis of Fe_3O_4 @ SiO_2 -EP-NH-HPA (IV) nanocatalyst

General procedure for the preparation of $\text{H}_3\text{PW}_{12}\text{O}_{40}$ loaded on the magnetic core of $\text{Fe}_3\text{O}_4@\text{SiO}_2\text{-EP-NH}$

$\text{Fe}_3\text{O}_4@\text{SiO}_2\text{-EP-NH}$ (1 g) was suspended in a methanolic solution of phosphotungstic acid (1 g in 50 mL), and the mixture was briefly sonicated and then stirred at 60 °C for 24 h. The resulting solid was separated with an external magnet and repeatedly washed with MeOH and dried at 60 °C for 8 h and designated as $\text{Fe}_3\text{O}_4@\text{SiO}_2\text{-EP-NH-HPA}$. The total synthesis is summarized in Scheme 3, Stage IV.

Catalytic activity

General procedure for the preparation of pyranopyrazoles

To a prestirred mixture of ethyl acetoacetate 1 (1 mmol) and hydrazine hydrate 2 (1 mmol) in 25 mL round-bottom flask in water (5 mL), various aromatic aldehydes 3(a–t) (1 mmol) and malononitrile 4 (1 mmol) along with $\text{Fe}_3\text{O}_4@\text{SiO}_2\text{-EP-NH-HPA}$ (20 mg) as a catalyst were added. The resulting mixture was stirred at room temperature for certain time periods as indicated in Table 4. After the reaction was completed (monitored by TLC: *n*-hexane–ethyl acetate, 4:1), water was removed from the reaction mixture under reduced pressure followed by dissolving the product in warm ethanol (5 mL). The catalyst was then separated using an external magnet and washed with ethanol and dried to be used in other reactions. Subsequently, the solvent (ethanol) was evaporated to afford the pure product. And finally, the isolated compounds were characterized by melting point analysis, FTIR, mass, ^1H NMR and ^{13}C NMR spectroscopy.

Physical and spectral data of some products

6-Amino-3-methyl-4-(4-nitrophenyl)-2,4-dihydropyrano[2,3-*c*]pyrazole-5-carbonitrile(5d) White solid; Mp: 249–251 °C; FTIR (KBr, cm^{-1}): 3477, 3284, 3229, 3118, 2196, 1650, 1594, 1401, 744; ^1H NMR (300 MHz, $\text{DMSO-}d_6$): δ (ppm) 1.82 (*s*, 3H, CH_3), 4.85 (*s*, 1H, Aliphatic-H), 7.08 (*s*, 2H, NH_2), 7.47–7.50 (*d*, 2H, Ar-H), 8.22–8.24 (*d*, 2H, Ar-H), 12.23 (*s*, 1H, NH). ^{13}C NMR (75 MHz, $\text{DMSO-}d_6$): δ (ppm) 10.22, 36.35, 56.37, 97.03, 120.96, 124.37, 129.31, 136.34, 146.85, 152.57, 155.14, 161.61. MS (ESI) m/z for (297).

6-Amino-3-methyl-4-(3-nitrophenyl)-2,4-dihydropyrano[2,3-*c*]pyrazole-5-carbonitrile(5e) White solid; Mp: 195–197 °C; IR (KBr, cm^{-1}): 3473, 3224, 3121, 2195, 1654, 1596, 1400, 733; ^1H NMR (300 MHz, $\text{DMSO-}d_6$): δ (ppm) 1.83 (*s*, 3H, CH_3), 4.90 (*s*, 1H, Aliphatic-H), 7.08 (*s*, 2H, NH_2), 7.64–7.71 (*m*, 2H, Ar-H), 8.05 (*s*, 1H, Ar-H), 8.13–8.17 (*m*, 1H, Ar-H), 12.23 (*s*, 1H, NH). ^{13}C NMR (75 MHz, $\text{DMSO-}d_6$): δ (ppm) 10.25, 36.12, 56.59, 97.14, 121.0, 122.32, 122.47, 130.73, 134.87, 136.37, 147.30, 148.35, 155.16, 161.61. MS (ESI) m/z for (297).

6-Amino-4-(4-cyanophenyl)-3-methyl-2,4-dihydropyrano[2,3-c]pyrazole-5-carbonitrile (5p) White solid; Mp: 228–230 °C; IR (KBr, cm^{-1}): 3480, 3284, 3111, 2228, 2188, 1641, 1492, 558; ^1H NMR (300 MHz, $\text{DMSO}-d_6$): δ (ppm) 1.81 (s, 3H, CH_3), 4.77 (s, 1H, Aliphatic-H), 7.05 (s, 2H, NH_2), 7.39–7.42 (dd, 2H, Ar-H), 7.81–7.84 (dd, 2H, Ar-H), 12.21 (s, 1H, NH); ^{13}C NMR (75 MHz, $\text{DMSO}-d_6$): δ (ppm) 10.20, 36.61, 56.48, 97.11, 110.09, 119.27, 121.0, 129.07, 133.08, 136.27, 150.53, 155.16, 161.59. MS (ESI) m/z for (276).

6-Amino-4-(5-bromo-2-hydroxyphenyl)-3-methyl-2,4-dihydropyrano[2,3-c]pyrazole-5-carbonitrile (5r) Pale yellow solid; Mp: 229–231 °C; IR (KBr, cm^{-1}): 3456, 3429, 3354, 3214, 2189, 1658, 1478; ^1H NMR (300 MHz, $\text{DMSO}-d_6$): δ (ppm) 2.05 (s, 3H, CH_3), 3.41 (s, 1H, OH), 4.66 (s, 1H, Aliphatic-H), 6.81 (s, 2H, NH_2), 6.95–6.98 (d, 1H, Ar-H), 7.15 (s, 1H, Ar-H), 7.35–7.38 (d, 1H, Ar-H), 10.56 (s-broad, 1H, NH); ^{13}C NMR (75 MHz, $\text{DMSO}-d_6$): δ (ppm) 10.3, 29.1, 55.2, 105.0, 116.0, 118.4, 121.0, 126.6, 130.8, 131.6, 137.1, 148.2, 159.5, 160.2. MS (ESI) m/z for (346). Elemental Analysis (CHN): C: 49.22, H: 3.46, N: 13.48%.

Results and discussion

Recently, the introduction and the designing of a better protocol for the synthesis of highly efficient and environmentally friendly novel heterogeneous catalysts with the use of green and safe reagents have become one of the most important parts of our ongoing research program. Based on the information obtained from the studies on *Equisetum arvense*, it was anticipated that this plant could be used as a plentiful source of silica with high surface area and high porosity [30]. So in this work, natural mesoporous silica with the high surface area was extracted and applied for the synthesis of $\text{Fe}_3\text{O}_4@\text{SiO}_2\text{-EP-NH-HPA}$ with core-shell nanostructure as a novel solid acid magnetic nanocatalyst (Scheme 2). The so-prepared magnetic nanocatalyst was fully characterized using various techniques such as FTIR, XRD, N_2 adsorption-desorption, TEM, SEM, EDX, TGA, VSM, ICP-OES and elemental analysis. The obtained results are summarized in the following sections in which all these techniques corroborate the successful preparation of the newly synthesized mesoporous catalyst.

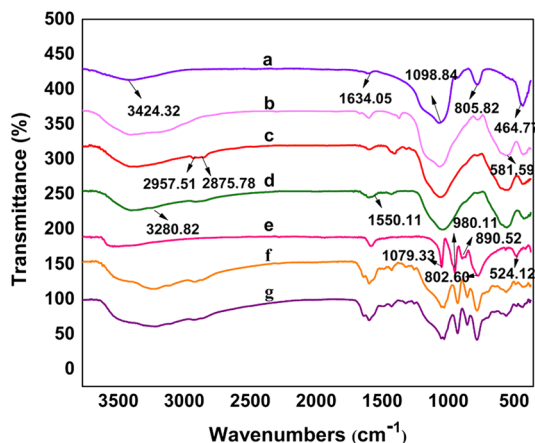
Characterization of novel $\text{Fe}_3\text{O}_4@\text{SiO}_2\text{-EP-NH-HPA}$

FTIR analysis

FTIR spectra are one of the methods which confirm the successful synthesis of the nanocatalysts; therefore, they were used to analyze the synthesis of every step of the nanocatalyst of this research. FTIR spectra of horsetail plant (*Equisetum arvense*) and extracted silica are shown in Fig. 1. In the case of horsetail plant (Fig. 1a), the peaks at 3460 and 1640 cm^{-1} are, respectively, attributed to the stretching and

Table 1 Specific surface area (S_{BET}), pore volume and mean pore diameter of horsetail plant, isolated silica, $\text{Fe}_3\text{O}_4@/\text{SiO}_2$ (I) and $\text{Fe}_3\text{O}_4@/\text{SiO}_2$ -EP-NH-HPA (IV)

Sample	S_{BET} ($\text{m}^2 \text{g}^{-1}$)	Total pore volume ($\text{cm}^3 \text{g}^{-1}$)	Mean pore diameter (nm)
Horsetail plant	2.025	0.0094	7.63
Isolated silica	450	0.66	8.12
$\text{Fe}_3\text{O}_4@/\text{SiO}_2$ (I)	245	0.56	6.77
$\text{Fe}_3\text{O}_4@/\text{SiO}_2$ -EP-NH-HPA (IV)	180	0.35	5.68

Fig. 2 FTIR spectra of **a** isolated silica, **b** $\text{Fe}_3\text{O}_4@/\text{SiO}_2$ (I), **c** $\text{Fe}_3\text{O}_4@/\text{SiO}_2$ -EP (II), **d** $\text{Fe}_3\text{O}_4@/\text{SiO}_2$ -EP-NH (III), **e** pure $\text{H}_3\text{PW}_{12}\text{O}_{40}$, **f** $\text{Fe}_3\text{O}_4@/\text{SiO}_2$ -EP-NH-HPA (IV) and **g** seventh reused $\text{Fe}_3\text{O}_4@/\text{SiO}_2$ -EP-NH-HPA

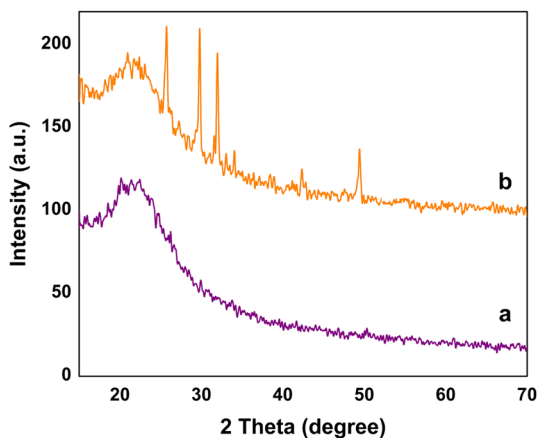
bending modes of the Si–OH groups and the adsorbed water [39, 40]. The doublet peaks appearing in the range of 2925 and 2855 cm^{-1} are characteristics of C–H stretching vibrations, which prove the existence of aliphatic compounds in this plant [41]. There is also a weak peak around 1734 cm^{-1} , which was proposed to be attributed to the C=O stretching of the related organic compounds [42]. The depicted strong peaks at 1100, 813 and 468 cm^{-1} are assigned to Si–O–Si asymmetric stretching, symmetric stretching and bending modes of silica, respectively [43], which prove the presence of silica. This plant is regarded as a rich source of silica; however, the presence of organic compounds and other metals causes the plant to have a very small surface area (2.02 m^2/g , Table 1), which limits its use as support and further functionalization. As a result, we decided to extract pure silica having a high surface area from the plant (450 m^2/g , Table 1). The FTIR spectrum presented in Fig. 1b shows three significant peaks in 1098, 805 and 464 cm^{-1} that confirms all peaks that were related to the organic compounds have been lost and pure silica was well synthesized. Furthermore, EDX analysis was carried out to prove that metal constituents have been removed successfully from the plant (Fig. 9b). The FTIR spectra of the final nanocatalyst which was synthesized in six steps along with the seventh reused nanocatalyst are demonstrated in Fig. 2. As can be seen, Fig. 2a presents the FTIR spectrum of synthesized pure silica mentioned above. As presented in Fig. 2b, the main characteristic bond adsorption for the formation of

iron nanoparticles is observed in the area of 581 cm^{-1} related to the stretching vibration of the Fe–O band [44]. Also, peaks observed at 1098 and 805 cm^{-1} which can be correlated with the asymmetric and symmetric stretching of Si–O–Si confirm the presence of silica coatings on the Fe_3O_4 nanoparticles. Successful coupling of epoxy rings to the surface of silica-coated magnetic nanoparticles was demonstrated by the stretching vibration of aliphatic CH_2 groups of epibromohydrin at 2957 and 2875 cm^{-1} and C–O–C vibration stretching at 1240 – 1260 cm^{-1} [45]. In this case, the vibration frequency of C–O–C was covered by the asymmetric vibration of the Si–O–Si band. These results indicated that the $\text{Fe}_3\text{O}_4@\text{SiO}_2$ surface had been immobilized by covalent-bonded organic epoxy rings (Fig. 2c). Furthermore, the ring opening of the epoxy ring with ethylenediamine was asserted by appearance of the absorption broad bands around 3280 and 1550 cm^{-1} corresponding to the N–H stretching and bending vibrations, respectively, which confirm the successful functionalization of the $\text{Fe}_3\text{O}_4@\text{SiO}_2\text{-EP}$ with ethylenediamine (Fig. 2d) [46]. In Fig. 2e, pure $\text{H}_3\text{PW}_{12}\text{O}_{40}$ with a Keggin structure shows four strong bands at 1079 cm^{-1} (P–O), 980 cm^{-1} (W–O), the bands at 890 cm^{-1} and 802 cm^{-1} (W–O–W) and one weak band at 524 cm^{-1} (W–O–P) [47]. As shown in the FTIR spectrum of final nanocatalyst (Fig. 2f), after supporting the $\text{H}_3\text{PW}_{12}\text{O}_{40}$ on the $\text{Fe}_3\text{O}_4@\text{SiO}_2\text{-EP-NH}$, the above-mentioned diagnostic vibrational peaks could be still found in the FTIR spectrum. Also, the vibrations of tetrahedral P–O bonds of Keggin units may overlap with the characteristic asymmetric stretching modes of Si–O bonds in the SiO_2 structure (at 1098 cm^{-1}) [48]. As depicted in Fig. 2g, the FTIR spectrum of the $\text{Fe}_3\text{O}_4@\text{SiO}_2\text{-EP-NH-HPA}$ nanocatalyst demonstrates that almost no change occurs after being used seven times.

X-ray diffraction analysis

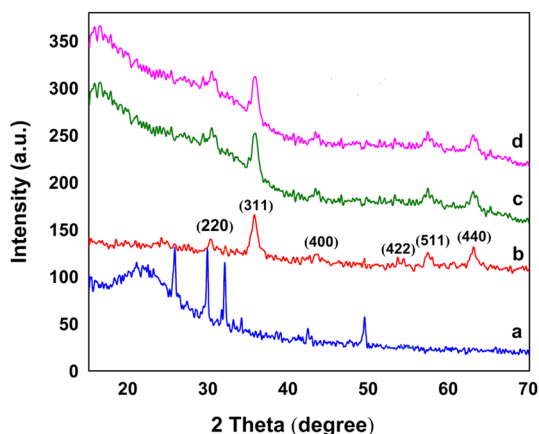
The crystalline phase and purity of the synthesized material were indicated by the powder XRD patterns. First, the crystallinity of silica in horsetail plant

Fig. 3 XRD patterns of **a** horsetail plant and **b** extracted silica



(*Equisetum arvense*) and silica derived from HCl treatment followed by calcination is studied by X-ray diffraction. In horsetail plant (Fig. 3a), a broad peak appeared around 2θ equal to 22° indicating that the silica of the plant was mainly in the form of amorphous [49]. As can be seen in Fig. 3b, silica extracted from *Equisetum arvense* after HCl treatment followed by calcination shows several crystalline peaks attributed to α -quartz besides a prominent broad peak of amorphous silica based on the powder diffraction pattern [50]. Quartz is the only crystalline component detected in these samples. The crystalline nature of $\text{Fe}_3\text{O}_4@\text{SiO}_2$ along with X-ray diffraction patterns of $\text{Fe}_3\text{O}_4@\text{SiO}_2\text{-EP-NH-HPA}$ and the seventh recovered $\text{Fe}_3\text{O}_4@\text{SiO}_2\text{-EP-NH-HPA}$ is demonstrated in Fig. 4. According to curve 4b, six characteristic peaks at the values of 2θ equal to 30.4 (220), 35.8 (311), 43.8 (400), 54.2 (422), 57.2 (511) and 62.8 (440) correspond to the characteristic peaks of cubic structure Fe_3O_4 MNPs (JCPDS: 19-0629) [51], revealing a high phase purity of magnetite. Also, a new broad peak at $2\theta=22$ related to the amorphous silica shell together with some crystalline α -quartz peaks with low intensity was observed. The mean crystalline sizes of Fe_3O_4 nanoparticles are calculated to be 30 nm using Debye–Scherrer’s equation. As illustrated in Fig. 4c, despite the immobilization of organic segment and forming of $\text{Fe}_3\text{O}_4@\text{SiO}_2\text{-EP-NH-HPA}$, the crystallinity of Fe_3O_4 nanoparticles is well retained throughout the process, and in comparison with curve 4b, no remarkable change occurred in the number of peaks in curve 4c. In addition, due to its dispersion in the catalyst matrix, $\text{H}_3\text{PW}_{12}\text{O}_{40}$ showed no peaks in the XRD pattern. Hence, it can be concluded that immobilization of $\text{H}_3\text{PW}_{12}\text{O}_{40}$ nanoparticles cannot lead to disruption of the formation of a regular catalyst crystal network. The presence of $\text{H}_3\text{PW}_{12}\text{O}_{40}$ nanoparticles was verified through the analysis of ICP and EDX techniques. The obtained results achieved from the XRD pattern of the seventh recovered $\text{Fe}_3\text{O}_4@\text{SiO}_2\text{-EP-NH-HPA}$ nanocatalyst indicate that there was no significant difference in the chemical structure of catalyst before and after seven times reuse (Fig. 4d).

Fig. 4 XRD patterns of **a** extracted silica, **b** $\text{Fe}_3\text{O}_4@\text{SiO}_2$ NPs (**I**), **c** $\text{Fe}_3\text{O}_4@\text{SiO}_2\text{-EP-NH-HPA}$ (**IV**) and **d** seventh reused $\text{Fe}_3\text{O}_4@\text{SiO}_2\text{-EP-NH-HPA}$ (**IV**)



N₂ adsorption–desorption studies

The structural and textural properties of isolated silica and Fe₃O₄@SiO₂-EP-NH-HPA (IV) were investigated through the N₂ adsorption and desorption isotherms results. The nitrogen sorption isotherm of isolated silica (Fig. 5a) shows a typical type IV isotherm with an H1 hysteresis loop, indicating the characteristic of mesoporous silica network [52]. Furthermore, the corresponding pore-size distribution from a BJH analysis of the sorption isotherms shows a narrow size distribution peaked at around 6 nm (Fig. 5b). In addition, the adsorption–desorption curve for Fe₃O₄@SiO₂-EP-NH-HPA (Fig. 5c) displayed the characteristics of type II isotherm with H3-type hysteresis loop demonstrating the existence of mesoporous or macroporous structure according to the IUPAC classification [53]. Moreover, the BJH calculations revealed a uniform pore-size distribution accompanied by a high-intensity peak, which ascertains the high-regularity pore-size distribution for

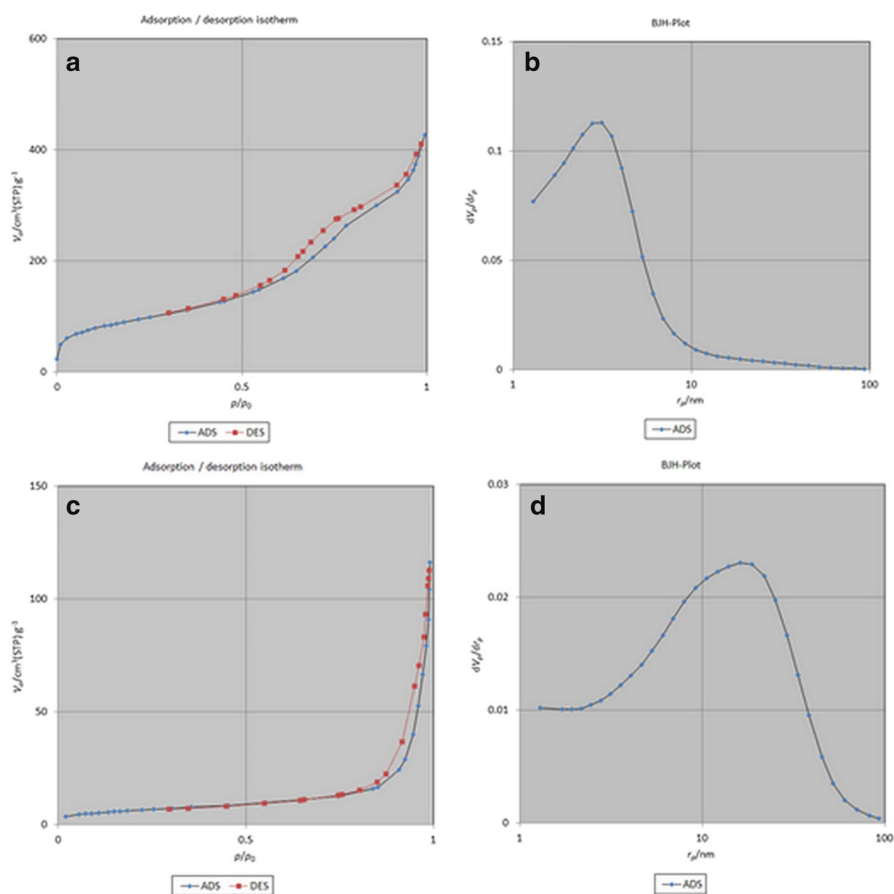


Fig. 5 N₂ adsorption–desorption isotherms and pore-size distributions for **a, b** isolated silica and **c, d** Fe₃O₄@SiO₂-EP-NH-HPA (IV), respectively

nanocatalyst (Fig. 5d). The specific surface areas and pore volume and mean pore diameter of horsetail plant, isolated silica, $\text{Fe}_3\text{O}_4@\text{SiO}_2$ and $\text{Fe}_3\text{O}_4@\text{SiO}_2\text{-EP-NH-HPA}$ were determined by applying the BET equation, and the numerical data are listed in Table 1. As shown in Table 1, the isolated silica sample had a maximum specific surface area of $450 \text{ m}^2 \text{ g}^{-1}$ in comparison with native horsetail, and all of the functionalized materials had a smaller surface area, pore size and pore volume, which can be easily realized due to the fact that the occupation of some pores by anchored organic segments carried out successfully.

TEM analysis

The size and morphology of $\text{Fe}_3\text{O}_4@\text{SiO}_2\text{-EP-NH-HPA}$ nanocatalyst were investigated by TEM technique corroborating the homogeneous spherical core-shell morphology for $\text{Fe}_3\text{O}_4@\text{SiO}_2\text{-EP-NH-HPA}$ (Fig. 6a, b). Moreover, the TEM image of seventh reused $\text{Fe}_3\text{O}_4@\text{SiO}_2\text{-EP-NH-HPA}$ catalyst, shown in Fig. 6c, d revealed that

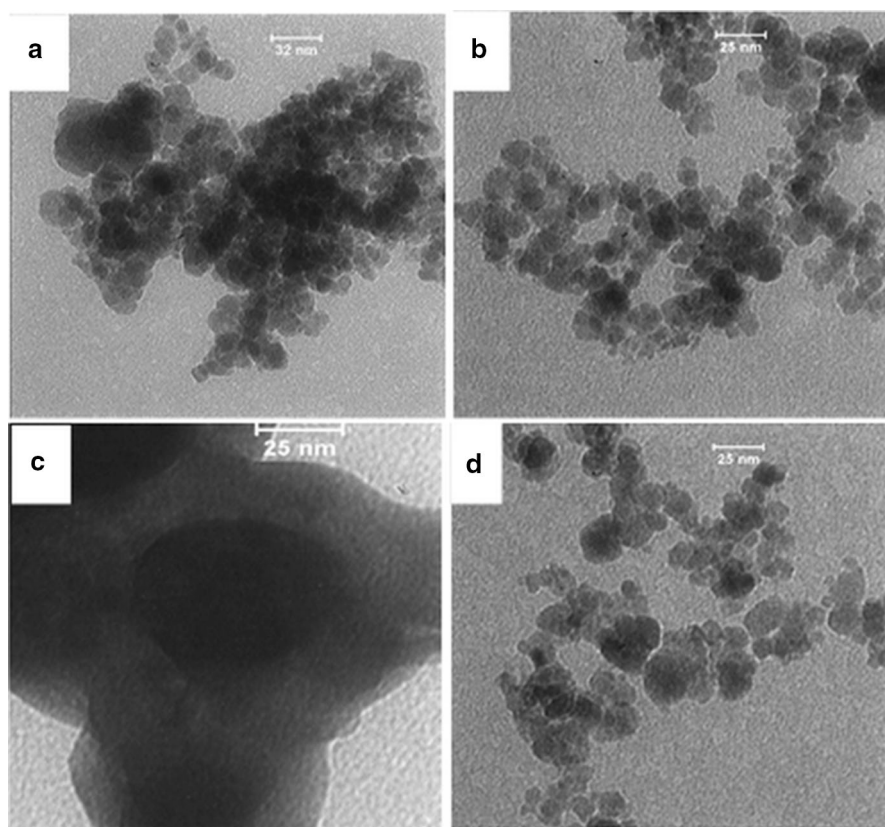
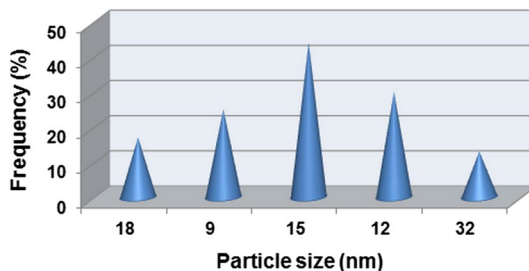


Fig. 6 TEM image of **a, b** $\text{Fe}_3\text{O}_4@\text{SiO}_2\text{-EP-NH-HPA}$ (**IV**) and **c, d** seventh reused $\text{Fe}_3\text{O}_4@\text{SiO}_2\text{-EP-NH-HPA}$ (**IV**)

Fig. 7 Particle size distribution histogram of $\text{Fe}_3\text{O}_4@\text{SiO}_2\text{-EP-NH-HPA}$ (IV)



no significant change was detected in the morphology of the catalyst even after seven recoveries. Also, particle size distribution histogram of the nanocatalyst which was calculated according to the TEM analysis is presented in Fig. 7. This diagram was obtained by measuring 150 separated particles and displayed that the particle sizes of $\text{Fe}_3\text{O}_4@\text{SiO}_2\text{-EP-NH-HPA}$ in irregular geometric shape were about 9–32 nm and the average diameter of the nanoparticles was about 15 nm. The attained TEM results were in accordance with the small-angle XRD, as well as with data obtained from nitrogen adsorption–desorption analyses.

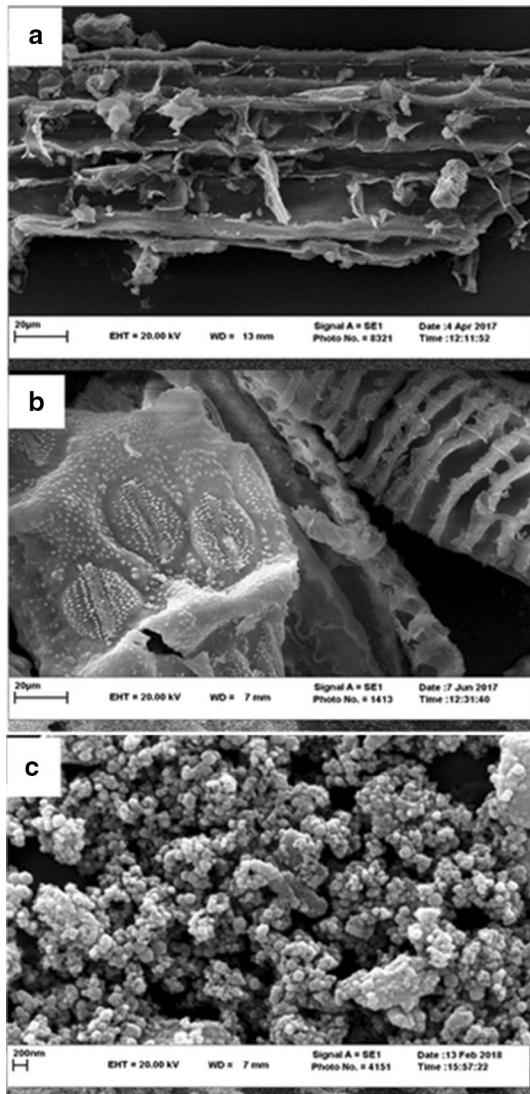
SEM analysis

The size and surface morphology of native horsetail plant, isolated silica and $\text{Fe}_3\text{O}_4@\text{SiO}_2\text{-EP-NH-HPA}$ catalyst were further determined using emission scanning electron microscopy (SEM). As illustrated in Fig. 8, silicon was found at its highest amount in the outer edge of both native horsetail plant and isolated silica (Fig. 8a, b, respectively). The results presented by the SEM image of isolated silica (Fig. 8b), which were achieved through HCl treatment followed by calcination and resulted in elimination of mineral and organic compounds, surprisingly illustrated that the original structure of horsetail plant was still perfectly retained even though the merging of its rows has occurred owing to shrinkage, indicating that the accumulation of silica over the whole outer surface forms a continuous layer of siliceous. SEM images of the prepared nanocatalyst reveal that the core–shell nanoparticles have spherical morphology with uniform size (Fig. 8c). Also, resulting images indicate that the sizes of the catalyst particles are on the nanometer scale having a mean diameter of about 9–32 nm with good disparity. These results are in good accordance with the particle size extracted from the XRD, TEM and nitrogen adsorption–desorption analyses.

EDX analysis

Energy-dispersive X-ray spectroscopy (EDX) was conducted as another powerful tool to completely confirm the successful synthesis of all steps of catalyst. The EDX spectrum of horsetail (*Equisetum arvense*) (Fig. 9a) shows the presence of high concentrations of carbon related to organic compounds (e.g., cellulose, hemicellulose, pectin) and alkali and alkaline-earth metals, for instance Si, Ca, K, Mg, S, Al, as

Fig. 8 SEM images of **a** horse-tail plant, **b** isolated silica and **c** $\text{Fe}_3\text{O}_4@\text{SiO}_2\text{-EP-NH-HPA}$ (IV) MNPs



the main components [29]; however, the concentration of silica was revealed to be higher than that of other metals. To extract silica with high surface area, HCl treatment followed by calcination was performed on *Equisetum arvense* to completely remove all inorganic and organic compounds except silica. Figure 9b reveals the successful synthesis of silica, and it is worth noting that no impurity elements were detected in the structure. The EDX spectrum of $\text{Fe}_3\text{O}_4@\text{SiO}_2\text{-EP-EN-HPA}$ (IV) (Fig. 9c) shows the presence of Si, C, Fe, P, N and W proving the successive surface functionalization of the silica-encapsulated magnetite nanoparticles, which confirms the structure of the final nanocatalyst.

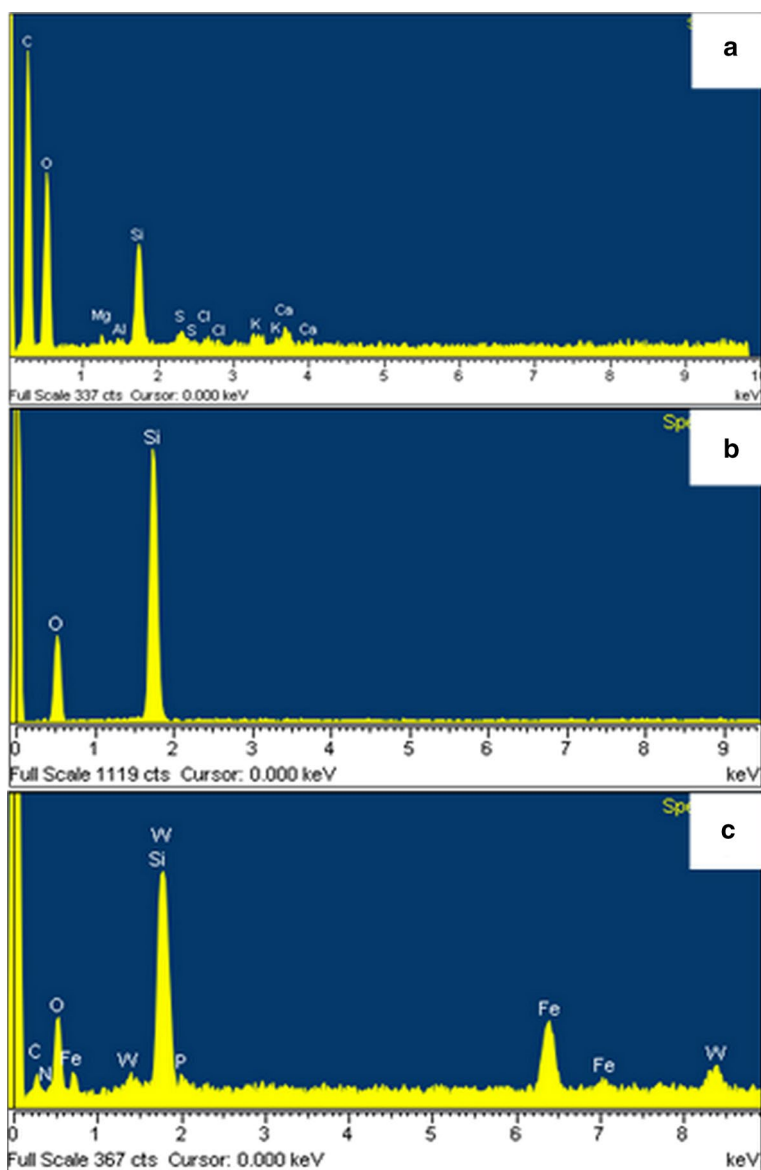
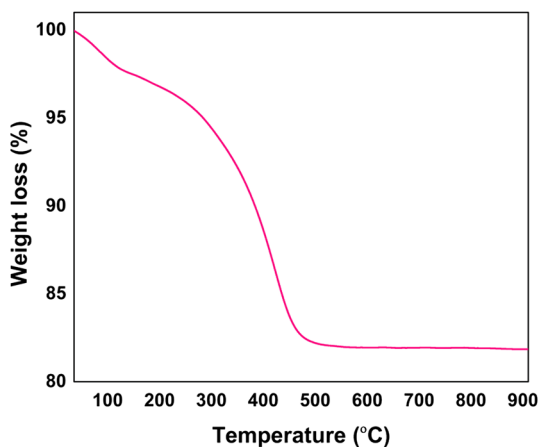


Fig. 9 EDX analysis of **a** horsetail plant, **b** isolated silica and **c** $\text{Fe}_3\text{O}_4@ \text{SiO}_2\text{-EP-NH-HPA (IV)}$ MNPs

Thermal analysis

To determine the thermal stability of $\text{Fe}_3\text{O}_4@ \text{SiO}_2\text{-EP-NH-HPA}$ as well as the percent of organic functional groups attached to the surface of the magnetic nanoparticles, thermogravimetric analysis (TGA) was conducted and the obtained curve is illustrated in Fig. 10. The TGA plot of $\text{Fe}_3\text{O}_4@ \text{SiO}_2\text{-EP-NH-HPA}$ depicts two main

Fig. 10 TGA thermogram of $\text{Fe}_3\text{O}_4@\text{SiO}_2\text{-EP-NH-HPA}$ (**IV**)



weight loss steps from the samples in the temperature range of 30–600 °C. As can be seen, the first weight loss of about 3% at a temperature below 200 °C was related to the removal of physically trapped water molecules and the second weight loss of about 15% in the temperature range of 200–600 °C was attributed to the thermal decomposition of the organic parts that were grafted on the surface of the nanocatalyst [54]. Based on TGA results, the amount of organic segments supported on $\text{Fe}_3\text{O}_4@\text{SiO}_2$ MNPs is estimated to be 1.2 mmol g^{-1} , which is in good agreement with the results obtained via elemental analysis data (CHNs). These results presented in Table 2 confirmed the loading amount of organic layer immobilized on $\text{Fe}_3\text{O}_4@\text{SiO}_2$ was 1.2 mmol g^{-1} ($C=2.36\%$, $N=2.25\%$), demonstrating that organic ligand attached successfully to the surface of $\text{Fe}_3\text{O}_4@\text{SiO}_2$ core–shell NPs.

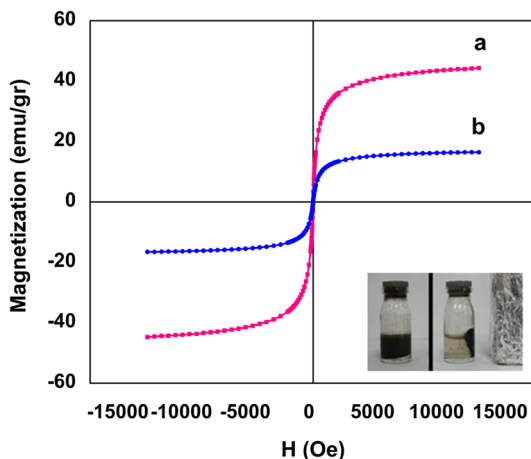
Magnetic measurement

Paramagnetic particles are highly valuable for their magnetic separation, so the magnetic behavior of $\text{Fe}_3\text{O}_4@\text{SiO}_2$ and $\text{Fe}_3\text{O}_4@\text{SiO}_2\text{-EP-NH-HPA}$ nanocatalyst was carried out by VSM (vibrating sample magnetometer) technique at room temperature. As shown in Fig. 11, the saturated magnetization values of $\text{Fe}_3\text{O}_4@\text{SiO}_2$ (Fig. 11a) and $\text{Fe}_3\text{O}_4@\text{SiO}_2\text{-EP-NH-HPA}$ (Fig. 11b) are 44, and 16.5 emu/g, respectively. Compared to $\text{Fe}_3\text{O}_4@\text{SiO}_2$ NPs, the saturation magnetization intensity of $\text{Fe}_3\text{O}_4@\text{SiO}_2\text{-EP-NH-HPA}$ NPs was decreased, which was ascribed to organic functional

Table 2 Thermogravimetric analysis (TGA) and elemental analysis (EA) results

Sample	Percentage of weight loss (%)	Organic grafted segments (mmol g^{-1})	Elemental analysis (%)	
			C	N
$\text{Fe}_3\text{O}_4@\text{SiO}_2\text{-EP-NH-HPA}$	15	1.2	2.36	2.25

Fig. 11 Magnetization curves of **a** $\text{Fe}_3\text{O}_4@\text{SiO}_2$ (**I**) and **b** $\text{Fe}_3\text{O}_4@\text{SiO}_2\text{-EP-NH-HPA}$ (**IV**)



groups grafted on the surface of $\text{Fe}_3\text{O}_4@\text{SiO}_2$. It is worth pointing out that $\text{Fe}_3\text{O}_4@\text{SiO}_2\text{-EP-NH-HPA}$ still maintained a good magnetism and could be separated easily by an external magnet from the reaction mixture, which is important for the magnetic separation and reusability of the magnetic catalyst. Also, it is worth mentioning that no remarkable hysteresis, remanence or coercivity was detected in the magnetization curves revealing superparamagnetic properties for nanocatalyst resulting in easy separation from the reaction system [55, 56].

ICP-OES analysis

Inductively coupled plasma optical emission spectroscopy (ICP-OES) analysis was applied to realize the exact amount of tungsten in the fresh and reused nanocatalyst. This technique showed that 0.42 and 0.40 mmol of tungsten were anchored on 1.000 g of the fresh and seventh reused nanocatalyst, respectively. According to the obtained results, no significant leaching of tungsten from the surface of $\text{Fe}_3\text{O}_4@\text{SiO}_2\text{-EP-NH-HPA}$ NPs was observed even after seven recycle runs.

Application of $\text{Fe}_3\text{O}_4@\text{SiO}_2\text{-EP-NH-HPA}$

After characterizing the newly prepared nanocatalyst, it was aimed to investigate its catalytic activity, as a magnetically recyclable heterogeneous solid acid nanocatalyst for the one-pot four-component synthesis of dihydropyrano[2,3-*c*]pyrazole derivatives. First of all, in order to achieve the optimum conditions for this reaction, model substrates ethyl acetoacetate (1 mmol), hydrazine hydrate (1 mmol), malononitrile (1 mmol), and 4-nitrobenzaldehyde (1 mmol) were selected and various parameters such as the amount of catalyst, reaction temperature, reaction time, type of solvent system as well as solvent-free conditions were evaluated. The results of all optimization experiments for the model reaction are listed in Table 3. The completions of the reactions were monitored by TLC. As can be seen, the best result was obtained using 20 mg of $\text{Fe}_3\text{O}_4@\text{SiO}_2\text{-EP-NH-HPA}$ (**IV**) at room temperature in an aqueous

Table 3 One-pot, four-component synthesis of 6-amino-3-methyl-4-(4-nitrophenyl)-2,4-dihydropyrano[2,3-c]pyrazole-5-carbonitrile(5d) under different reaction conditions

Entry	Catalyst(g)	Solvent	T (°C)	Time (min)	Conversion %
1	–	–	100	120	< 5
2	Fe ₃ O ₄ @SiO ₂ -EP-NH-HPA (0.005)	Water	25	35	52
3	Fe ₃ O ₄ @SiO ₂ -EP-NH-HPA (0.02)	Water	25	3	99
4	Fe ₃ O ₄ @SiO ₂ -EP-NH-HPA (0.02)	Water	70	3	99
5	Fe ₃ O ₄ @SiO ₂ -EP-NH-HPA (0.04)	Water	25	3	99
6	Fe ₃ O ₄ @SiO ₂ -EP-NH-HPA (0.02)	EtOH	25	25	78
7	Fe ₃ O ₄ @SiO ₂ -EP-NH-HPA (0.02)	MeCN	25	20	85
8	Fe ₃ O ₄ @SiO ₂ -EP-NH-HPA (0.02)	–	25	120	< 30
9	Isolated SiO ₂ (0.02)	Water	25	55	0
10	Fe ₃ O ₄ (0.02)	Water	25	35	85
11	H ₃ PW ₁₂ O ₄₀ (0.02)	Water	25	50	45

medium (Table 3, entry 3). When the amount of catalyst was lower, the yield of the product decreased (Table 3, entry 2). Further increase in the amount of catalyst had no effects on the yield and the reaction time (Table 3, entry 5), and also, in the absence of catalyst, lower product yield was observed, even after prolonged reaction time (Table 3, entry 1). For choosing the reaction media, various solvents such as H₂O, EtOH and MeCN and also solvent-free conditions were used. In these experiments, the most promising result was obtained when water was employed as the solvent; therefore, water was selected as the encouraging solvent for the reaction. Then, to optimize the reaction temperature, three different temperatures (25, 70 and 100 °C) were employed for the reaction and the best result was obtained at 25 °C. By increasing the temperature from 25 to 100 °C, no noticeable increase in the yield was observed. Furthermore, to estimate the effect of the nanocatalyst species on the reaction progress, isolated SiO₂, Fe₃O₄ and H₃PW₁₂O₄₀ were separately used as catalysts in the model reaction under similar optimized conditions (Table 3, entries 9, 10, 11). The catalytic performance of Fe₃O₄ as catalyst was checked in model reaction indicating that Fe₃O₄ due to having Lewis acidic properties could produce the product in trace amounts. (Table 3, entry 10). Further analyses of the results pointed out that when isolated SiO₂ was used separately as a catalyst in model reaction, no product was obtained revealing the fact that just having high surface area is not sufficient for promoting model reaction and this clearly showed that the reaction was catalyzed by the acidic moiety (Table 3, entry 9). Moreover, by keeping the other conditions the same, the effectiveness of applying pure H₃PW₁₂O₄₀ as a catalyst was also investigated. However, the result was far from satisfactory in this context (Table 3 entry 11). Even though HPA is a homogenous strong acid in nature and is expected to have more activity, the catalytic activity of Fe₃O₄@SiO₂-EP-NH-HPA (IV) was a great deal higher and provided better results due to its conversion to nanometric counterpart. Therefore, the immobilization of HPA is highly effective in reaction progress due to having more surface atoms in comparison with the conventional one which results in more activity of the designed catalyst.

After optimization of the reaction conditions, in order to determine and investigate the scope and efficiency of the novel synthesized $\text{Fe}_3\text{O}_4@\text{SiO}_2\text{-EP-NH-HPA}$ (IV) as the next step, the focus of the study turned to apply this nanocatalyst in the synthesis of a series of 6-amino-2,4-dihydropyrano[2,3-c]pyrazol-5- carbonitrile derivatives. As a result, this catalyst was added (under optimized condition mentioned before) to a mixture of ethyl acetoacetate 1, hydrazine hydrate 2 in the reaction with various aromatic aldehydes 3 and malononitrile 4 in water (5 mL) at room temperature, to afford the corresponding products in high yields and in short reaction times (Table 4). Interestingly, a variety of aryl aldehydes bearing electron-withdrawing or electron-donating substituents (ortho-, meta- and para-substituted) were very encouraging in this reaction and gave the product in good to excellent yield (89–99%). In addition, using benzaldehydes with electron-withdrawing groups (at C4), the product was obtained in higher yields. This was achieved because, in the first step of the reaction mechanism, electron-withdrawing groups facilitated the nucleophilic addition to the carbonyl position of the aromatic aldehyde. Evidently, electron-releasing groups at C4 decreased the yield of the final product. It is worth mentioning that the formation and purity of products were confirmed by their melting point determination being in good accordance with the literature values and the structures of some of the products were well characterized by using FTIR, mass, ^1H NMR and ^{13}C NMR spectral data.

Finally, in order to compare the efficiency of this synthesized magnetic nanocatalyst with some of the other previously explored methods for this MCR, a comparison was made and the model reaction of ethyl acetoacetate, hydrazine hydrate, malononitrile and 4-Nitro benzaldehyde was considered as a representative example, and the results are classified in Table 5. As shown in Table 5, $\text{Fe}_3\text{O}_4@\text{SiO}_2\text{-EP-NH-HPA}$ (IV) has remarkably improved the synthesis of pyrano[2,3-c]pyrazole derivatives and acted convincingly superior over the reported methods concerning the reaction time and exhibited broad applicability in terms of yields.

Based on the research findings, one can propose a plausible synergic catalytic mechanism for the synthesis of dihydropyrano[2,3-c] pyrazole derivatives in the presence of $\text{Fe}_3\text{O}_4@\text{SiO}_2\text{-EP-NH-HPA}$ (IV) by the literature illustrated in Scheme 4 [63, 73]. It is believed that the reaction proceeds in a catalytic cycle which involves the synthesis of pyrazolone intermediate, Knoevenagel condensation, Michael addition and then intramolecular cyclization. As presented in scheme 4, both condensation of ethyl acetoacetate (A) with hydrazine hydrate (B) and the Knoevenagel condensation of the aryl aldehyde (C) with the nitrile anion (E) formed by the removal of acidic hydrogen from malononitrile were simultaneously promoted to produce the pyrazolone (G) and the intermediate olefin (F). Intermediate (G) was enolized in the presence of the catalyst to form compound (H). Subsequent Michael-type addition of (H) and (F) in the presence of the catalyst resulted in the in situ formation of intermediate (I). Finally, it underwent an intramolecular cyclization followed by tautomerization so that it could afford the desired dihydropyrano[2,3-c] pyrazole derivatives (J).

Table 4 Synthesis of pyrano[2,3-c]pyrazole derivatives catalyzed by $\text{Fe}_3\text{O}_4@ \text{SiO}_2\text{-EP-NH-HPA}(\text{IV})$

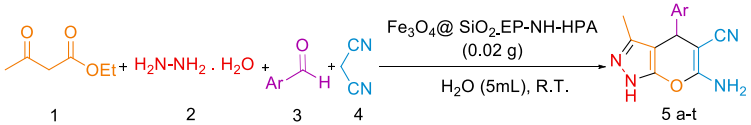
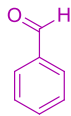
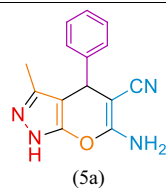
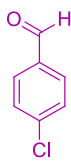
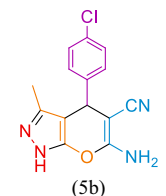
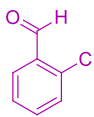
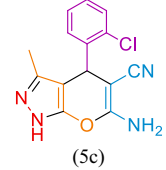
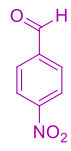
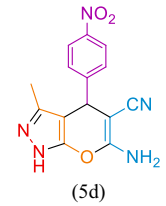
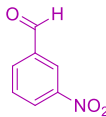
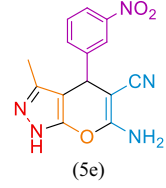
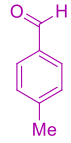
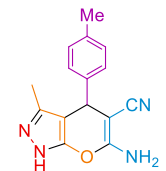
					
Entry	Aldehyde (Ar)	Product	Time (min)	Yield ^a (%)	M.P. ^b °C (Lit. References)
1		 (5a)	5	96	243–245 (245–256 [57])
2		 (5b)	4	99	233–235 (234–236 [58])
3		 (5c)	5	97	246–248 (247–248 [59])
4		 (5d)	3	99	249–251 (249–251 [60])
5		 (5e)	6	95	195–197 (194–196 [58])
6		 (5f)	7	91	206–207 (207–209 [61])

Table 4 (continued)

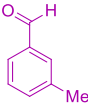
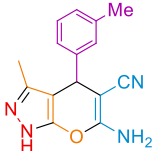
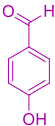
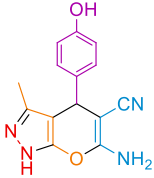
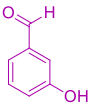
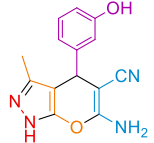
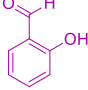
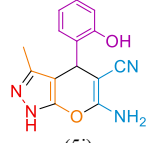
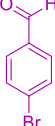
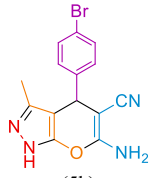
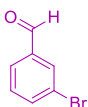
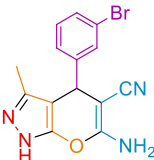
Entry	Aldehyde (Ar)	Product	Time (min)	Yield ^a (%)	M.P. ^b °C (Lit. References)
		(5f)			
7		 (5g)	8	90	172–174 (171–173 [62])
8		 (5h)	7	92	221–223 (220–221 [60])
9		 (5i)	6	91	254–256 (253–256 [63])
10		 (5j)	9	90	206–208 (204–205 [64])
11		 (5k)	3	96	179–181 (179–180 [57])
12		 (5l)	6	95	220–222 (218–220 [63])

Table 4 (continued)

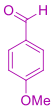
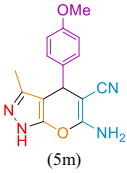
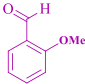
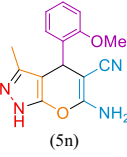
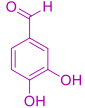
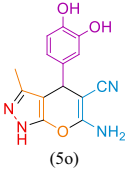
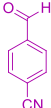
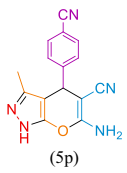
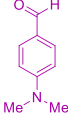
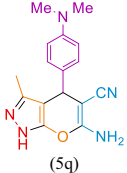
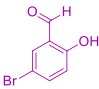
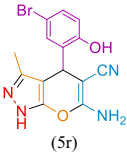
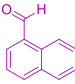
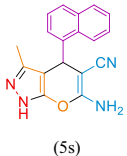
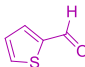
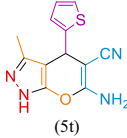
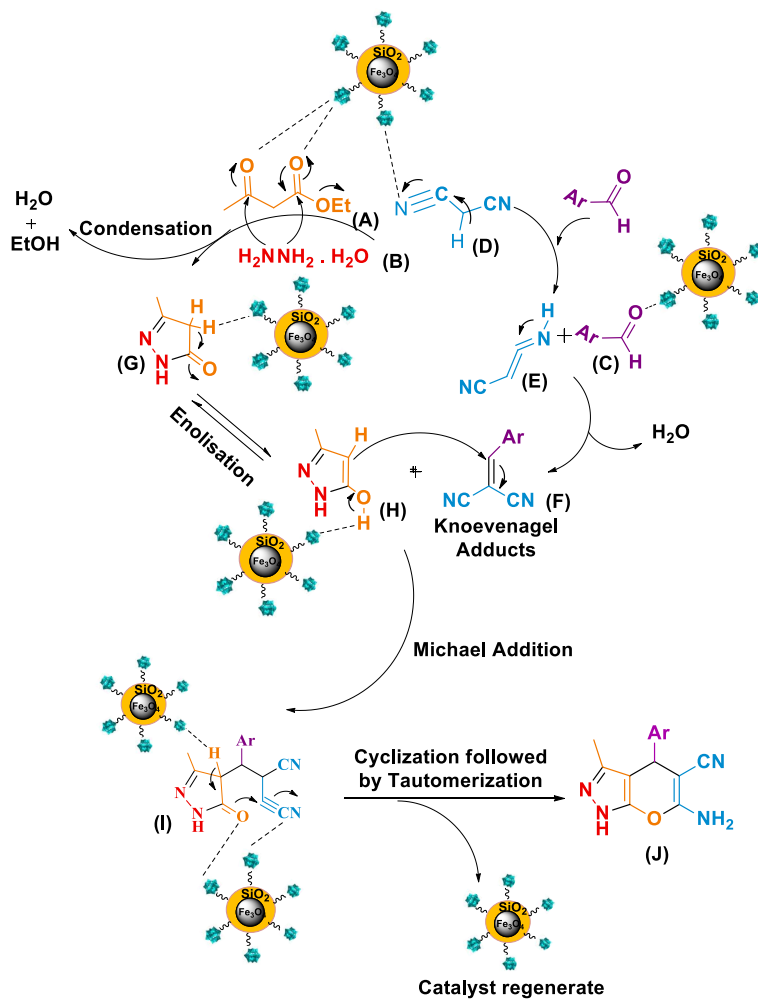
Entry	Aldehyde (Ar)	Product	Time (min)	Yield ^a (%)	M.P. ^b °C (Lit. References)
13		 (5m)	9	94	209–211 (211–212 [57])
14		 (5n)	10	93	251–253 (250–252 [65])
15		 (5o)	7	92	214–216 (215–217 [66])
16		 (5p)	6	97	228–230 (230–240 [63])
17		 (5q)	11	89	167–169 (162–164 [67])
18		 (5r)	10	96	229–231 (227–228 [57])
19		 (5s)	7	98	201–203 (200–201 [68])
20		 (5t)	6	90	190–192 (192–194 [59])

Table 5 Comparison of catalytic activity of $\text{Fe}_3\text{O}_4@\text{SiO}_2\text{-EP-NH-HPA (IV)}$ with other catalysts previously reported in the literature for synthesis of compound **5d**^a

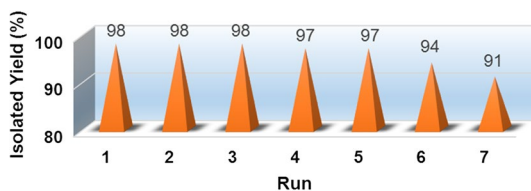
Entry	Catalyst	Reaction Condition	Time (min)	Yield ^b (%)	References
1	Organocatalyst ^c (5 mol%)	CH_2Cl_2 , rt.	14 h	88	[69]
2	γ -Alumina (30 mol%)	H_2O , reflux	40	85	[68]
3	SiO_2 TMG ^d (10 mol%)	100 °C, Neat	20	98	[65]
4	TUD ^e (10 mol%)	H_2O (5 mL), 80 °C	32	94	[57]
5	TBD-MSN ^f (10 mg)	Aq. EtOH, reflux	45	85	[70]
6	TiCl_4^g (10 mol%)	Solvent-free, 60 °C	50	84	[64]
7	MorT ^h (10 mol%)	$\text{EtOH}/\text{H}_2\text{O}$ (6 mL), reflux	6 h	92	[71]
8	Lemon juice (1 mL)	Water/ethanol (9:1, 10 mL), 90 °C	60	94	[72]
8	BSA ⁱ (50 mg)	$\text{EtOH}/\text{H}_2\text{O}$ (5 mL) at 45 °C	30	96	[60]
9	Electrolysis	EtOH , NaBr at 40 °C	25	90	[58]
10	Trisodium citrate dihydrate (10 mol%)	$\text{EtOH}/\text{H}_2\text{O}$ (1:1 v/v; 4 mL), rt.	2 h	85	[66]
11	SA ^j (15 mol%)	H_2O , reflux	5	88	[59]
12	Nano-[Fe-PSMP] Cl_2^k (4 mol%)	Solvent-free, 100 °C	5	88	[63]
13	$\text{Fe}_3\text{O}_4@\text{SiO}_2\text{-EP-NH-HPA}$ (0.02 g)	H_2O , rt.	3	99	This Work

^aReaction condition: 4-nitrobenzaldehyde (1 mmol), malononitrile (1 mmol), hydrazine hydrate (1 mmol) and ethyl acetoacetate (1 mmol)^bIsolated yield^cSome readily available cinchona alkaloid derivatives as the catalyst^dSilica-supported tetramethylguanidine^eThiourea dioxide^f1,5,7-Triazabicyclo-[4,4,0]-dec-1-ene (TBD)-anchored mesoporous silica nanoparticle^gTriaryl methyl chloride^hMorpholine triflateⁱBovine serum albumin^jSodium ascorbate^kNano-Fe-[phenylsalicylaldiminemethylpyranopyrazole] Cl_2



Scheme 4 Proposed mechanism for the preparation of the corresponding pyrano[2,3-c] pyrazole derivatives in the presence of $\text{Fe}_3\text{O}_4@\text{SiO}_2\text{-EP-NH-HPA}$ (IV)

Fig. 12 Synthesis of 6-amino-3-methyl-4-(4-nitrophenyl)-2,4-dihydropyrano[2,3-c]pyrazole-5-carbonitrile (**5d**) in the presence of reused $\text{Fe}_3\text{O}_4@\text{SiO}_2\text{-EP-NH-HPA}$ (IV)



Reusability of the catalyst

For practical applications of heterogeneous systems, the lifetime of the catalyst and its level of reusability are very important factors. In this regard, the reusability of $\text{Fe}_3\text{O}_4@\text{SiO}_2\text{-EP-NH-HPA}$ (IV) was investigated for the model reaction under optimized reaction conditions (Fig. 12). It is worth noting that in each process, after the completion of the reaction, the catalyst was easily recovered by the use of an external magnet, washed with ethanol and subsequently reused in the next run after being dried. It was realized that the nanocatalyst could be reused effectively for at least seven runs with insignificant deterioration in activity, which is ascribed to the stable functionalized groups on the catalyst. The obtained results from the FTIR (Fig. 2g), XRD pattern (Fig. 4d), TEM images (Fig. 6c, d) and ICP-OES analysis of the seventh recovered catalyst clearly indicated that there was not a great difference in the chemical structure of catalyst before and after seven runs.

Catalyst leaching study

In order to make sure that the catalytic activity of the nanocatalyst originated from immobilized functions within $\text{Fe}_3\text{O}_4@\text{SiO}_2\text{-EP-NH-HPA}$ (IV) and not from the drained segments, especially $\text{H}_3\text{PW}_{12}\text{O}_{40}$, in the reaction mixture, a leaching test was applied, and the results are presented in Fig. 13. To this aim, $\text{Fe}_3\text{O}_4@\text{SiO}_2\text{-EP-NH-HPA}$ (IV) (0.02 g) was added on model reaction under the optimized conditions. After having continued the reaction for 1.5 min, consequently, the catalyst was separated from the reaction mixture by the use of an external magnetic field, in which the product yield was reported to be 45%. Then, the resulting filtrate was allowed to react for a further 1.5 min, while the progress of the reaction was being monitored by TLC. Surprisingly, the results of the monitoring revealed that after the separation of the catalyst, almost no significant increase in the final conversion was observed. This affirmed the satisfactory steadiness of the $\text{Fe}_3\text{O}_4@\text{SiO}_2\text{-EP-NH-HPA}$ (IV) in the condensation reaction along with no destruction of the catalyst during the catalytic reaction. Also, these data suggested that $\text{H}_3\text{PW}_{12}\text{O}_{40}$ was strongly supported on the $\text{Fe}_3\text{O}_4@\text{SiO}_2\text{-EP-NH-HPA}$ (IV) network, and no leaching of $\text{H}_3\text{PW}_{12}\text{O}_{40}$ has been occurred confirming its accordance with the ICP-OES results.

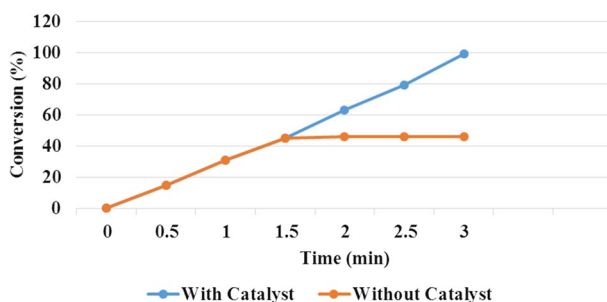


Fig. 13 Hot filtration test for the model reaction using $\text{Fe}_3\text{O}_4@\text{SiO}_2\text{-EP-NH-HPA}$ (IV)

Conclusion

To conclude, the findings of the current research revealed that the natural mesoporous SiO₂ having a high surface area can be easily extracted from horsetail plant as raw medicinal material and used for the first time as natural silica support. This natural silica, having an herbal origin, was applied to prepare Fe₃O₄@SiO₂-EP-NH-HPA (IV) as a magnetically heterogeneous solid acid nanocatalyst, which was then fully characterized by different analytical methods. The results obtained from the characterization confirmed the satisfactory synthesis of Fe₃O₄@SiO₂-EP-NH-HPA (IV) with spherical core-shell and mean diameters of 9–32 nm as a magnetic nanocatalyst. Subsequently, this green and newly synthesized nanocatalyst was applied for the one-pot synthesis of dihydropyrano[2,3-c] pyrazole derivatives, exhibiting excellent activity and stability, simple and effective separation using an appropriate external magnet leading to minimizing the loss of catalyst during separation and its reusability for several times with no significant loss of activity. It is recommended that the application of such synthetic methodology for using this medicinal plant with rich silica content, as a more practical alternative to the existing methods, is highly promising and provides a better scope for the preparation of pure silica by considering economical benefits, which would be in good accordance with the innovation of green chemistry.

Acknowledgements We are thankful to Ferdowsi University of Mashhad Research Council for financial support to this work (Grant No. p/3/45801).

Compliance with ethical standards

Conflict of interest The authors declare that they have no conflict of interest.

References

1. N.N. Sauer, *J. Am. Chem. Soc.* **122**, 5419 (2000)
2. V. Polshettiwar, R. Luque, A. Fihri, H. Zhu, M. Bouhrara, J.M. Basset, *Chem. Rev.* **111**, 3036 (2011)
3. S.M. Haile, D.A. Boysen, C.R.I. Chisholm, R.B. Merle, *Nature* **410**, 910 (2001)
4. N. Ahmed, Z.N. Siddiqui, *J. Mol. Catal. A Chem.* **387**, 45 (2014)
5. R. Pagadala, S. Maddila, V.D.B.C. Dasireddy, S.B. Jonnalagadda, *Catal. Commun.* **45**, 148 (2014)
6. I.V. Kozhevnikov, *J. Mol. Catal. A Chem.* **305**, 104 (2009)
7. H.J. Wang, X.N. Zhang, Z.H. Zhang, *Monatsh. Chem.* **141**, 425 (2010)
8. M. Kumaresan, K. Selvakumar, P. Sami, *Mater. Today Proc.* **4**, 12437 (2017)
9. G. Karthikeyan, A. Pandurangan, *J. Mol. Catal. A Chem.* **311**, 36 (2009)
10. L.T. Aany Sofia, A. Krishnan, M. Sankar, N.K.K. Raj, P. Manikandan, P.R. Rajamohanam, T.G. Ajithkumar, *J. Phys. Chem. C* **113**, 21114 (2009)
11. A. Hashemzadeh, M.M. Amini, R. Tayebbe, A. Sadeghian, L.J. Durndell, M.A. Isaacs, A. Osatiash-tiani, C.M.A. Parlett, A.F. Lee, *Mol. Catal.* **440**, 96 (2017)
12. E. Rafiee, M. Khodayari, S. Shahebrahimi, M. Joshaghani, *J. Mol. Catal. A Chem.* **351**, 204 (2011)
13. A. Ayati, M.M. Heravi, M. Daraie, B. Tanhaei, F.F. Bamoharram, M. Sillanpaa, *J. Iran. Chem. Soc.* **13**, 2301 (2016)
14. A. Jamshidi, B. Maleki, F. Mohammadi Zonoz, R. Tayebbe, *Mater. Chem. Phys.* **209**, 46 (2018)
15. P. Arora, J.K. Rajput, *Appl. Organomet. Chem.* **32**, e4001 (2018)

16. L. Cheng, X.P. Ye, *Catal. Lett.* **130**, 100 (2009)
17. S. Damyanova, J.L.G. Fierro, *Chem. Mater.* **10**, 871 (1998)
18. A. Micek-Ilnicka, E. Bielańska, L. Lityńska-Dobrzyńska, A. Bielański, *Appl. Catal. A Gen.* **421**, 91 (2012)
19. R. Mrówczyński, A. Nan, J. Liebscher, *RSC Adv.* **4**, 5927 (2014)
20. H. Veisi, P. Mohammadi, J. Gholami, *Appl. Organomet. Chem.* **28**, 868 (2014)
21. R. Liu, Y. Guo, G. Odusote, F. Qu, R.D. Priestley, *ACS Appl. Mater. Interfaces* **5**, 9167 (2013)
22. R.B. Nasir, R.S. Varma, A.C.S. Sustain, *Chem. Eng.* **2**, 2155 (2014)
23. A. Mobaraki, B. Movassagh, B. Karimi, *ACS Comb. Sci.* **16**, 352 (2014)
24. N. Nishiyama, S. Tanaka, Y. Egashira, Y. Oku, K. Ueyama, *Chem. Mater.* **15**, 1006 (2003)
25. V.B. Carmona, R.M. Oliveira, W.T.L. Silva, L.H.C. Mattoso, J.M. Marconcini, *Ind. Crops Prod.* **43**, 291 (2013)
26. P. Terzioğlu, S. Yucel, T.M. Rabagah, D. Özçimen, *BioRes.* **8**, 4406 (2013)
27. N. Nazriati, H. Setyawan, S. Affandi, M. Yuwana, S. Winardi, *J. Non Cryst. Solids* **400**, 6 (2014)
28. M.Y.N. Firdaus, H. Osman, H.S.C. Metselaar, A.R. Rozyanty, *BioRes.* **11**, 1270 (2016)
29. L. Sapei, Characterisation of silica in *Equisetum hyemale* and its transformation into biomorphous ceramics (2007), p. 1
30. G. Holzrüter, K. Narayanan, T. Gerber, *Bioanal. Chem.* **376**, 512 (2003)
31. D. Cloutier, A.K. Watson, *Weed Sci.* **33**, 358 (1985)
32. N. Radulović, G. Stojanović, R. Palić, *Phytother. Res.* **20**, 85 (2006)
33. N.S. Sandhu, S. Kaur, D. Chopra, *Asian J. Pharm. Clin. Res.* **3**, 146 (2010)
34. Z. Jieping, H. Bienayme, *Multicomponent Reactions* (Wiley, Weinheim, 2006), p. 76
35. D.J. Ramón, M. Yus, *Angew. Chem. Int. Ed.* **44**, 1602 (2005)
36. L. Weber, *Curr. Med. Chem.* **9**, 2085 (2002)
37. T. Ueda, H. Mase, N. Oda, I. Ito, *Chem. Pharm. Bull.* **29**, 3522 (1981)
38. S.C. Kuo, L.J. Huang, H. Nakamura, *J. Med. Chem.* **27**, 539 (1984)
39. F. Adam, K. Kandasamy, S. Balakrishnan, *J. Colloid Interface Sci.* **304**, 137 (2006)
40. R.A. Bini, R.F.C. Marques, F.J. Santos, J.A. Chaker, M. Jafellicci, *J. Magn. Magn. Mater.* **324**, 534 (2012)
41. B.M. Cherian, L.A. Pothan, T. Nguyen-Chung, G. Mennig, M. Kottaisamy, S. Thomas, *Agric. Food Chem.* **56**, 5617 (2008)
42. X.F. Sun, F. Xu, R.C. Sun, P. Fowler, M.S. Baird, *Carbohydr. Res.* **340**, 97 (2005)
43. L.D. White, C.P. Tripp, *J. Colloid Interface Sci.* **232**, 400 (2000)
44. J. Davarpanah, A.R. Kiasat, S. Noorizadeh, M. Ghahremani, *J. Mol. Catal. A Chem.* **376**, 78 (2013)
45. F. Adam, K.M. Hello, H. Osman, *Chin. J. Chem.* **28**, 2383 (2010)
46. A. Keivanloo, M. Bakherad, M. Khosrojerdi, A.H. Amin, *Res. Chem. Intermediat.* **44**, 2571 (2018)
47. X. Xie, J. Han, H. Wang, X. Zhu, X. Liu, Y. Niu, Z. Song, Q. Ge, *Catal. Today* **233**, 70 (2014)
48. F. Su, Q. Wu, D. Song, X. Zhang, M. Wang, Y. Guo, *J. Mater. Chem. A* **1**, 13209 (2013)
49. N. Yalcin, V. Sevinc, *Ceram. Int.* **27**, 219 (2001)
50. L. Sapei, R. Nöske, P. Strauch, O. Paris, *Chem. Mater.* **20**, 2020 (2008)
51. M. Esmailpour, A.R. Sardarian, J. Javidi, *Appl. Catal. A Gen.* **445–446**, 359 (2012)
52. M. Thommes, *Chem. Ing. Tech.* **82**, 1059 (2010)
53. M. Mora, C. Jiménez-Sanchidrián, J.R. Ruiz, *J. Colloid Interface Sci.* **302**, 568 (2006)
54. L. Moradi, M. Tadayon, *J. Saudi Chem. Soc.* **22**, 66 (2018)
55. L. Zhang, W.F. Dong, H.B. Sun, *Nanoscale* **5**, 7664 (2013)
56. A.R. Faraji, S. Mosazadeh, F. Ashouri, *J. Colloid Interface Sci.* **506**, 10 (2017)
57. R.H. Vekariya, K.D. Patel, H.D. Patel, *Res. Chem. Intermediat.* **42**, 4683 (2015)
58. A. Upadhyay, L.K. Sharma, V.K. Singh, R. Dubey, N. Kumar, R. Krishna Pal Singh, *Tetrahedron Lett.* **58**, 1245 (2017)
59. H. Kiyani, M. Bamdad, *Res. Chem. Intermediat.* **44**, 2761 (2018)
60. X. Huang, Z. Li, D. Wang, Y. Li, *Chin. J. Catal.* **37**, 1461 (2016)
61. H.R. Shaterian, K. Azizi, *Res. Chem. Intermediat.* **40**, 661 (2014)
62. F. Tamaddon, M. Alizadeh, *Tetrahedron Lett.* **55**, 3588 (2014)
63. A.R. Moosavi-Zare, H. Goudarziafshar, K. Saki, *Appl. Organomet. Chem.* **32**, e3968 (2018)
64. A.R. Moosavi-Zare, M.A. Zolfigol, A. Mousavi-Tashar, *Res. Chem. Intermediat.* **42**, 7305 (2016)
65. A.B. Atar, J.T. Kim, K.T. Lim, Y.T. Jeong, *Synth. Commun.* **44**, 2679 (2014)
66. G. Brahmachari, B. Banerjee, *Asian J. Org. Chem.* **5**, 271 (2016)
67. S.K. Shinde, M.U. Patil, S.A. Damate, S.S. Patil, *Res. Chem. Intermediat.* **44**, 1775 (2018)

68. H. Mecadon, M.R. Rohman, M. Rajbangshi, B. Myrboh, *Tetrahedron Lett.* **52**, 2523 (2011)
69. S. Gogoi, C.G. Zhao, *Tetrahedron Lett.* **50**, 2252 (2009)
70. B. Karmakar, *Aust. J. Chem.* **69**, 1117 (2016)
71. C.F. Zhou, J.J. Li, W.K. Su, *Chin. Chem. Lett.* **27**, 1686 (2016)
72. R.H. Vekariya, K.D. Patel, H.D. Patel, *Res. Chem. Intermediat.* **42**, 7559 (2016)
73. S. Paul, K. Pradhan, S. Ghosh, S.K. De, A.R. Das, *Tetrahedron* **70**, 6088 (2014)

Publisher's Note Springer Nature remains neutral with regard to jurisdictional claims in published maps and institutional affiliations.